Materials Chemistry and Physics 259 (2021) 124005

Contents lists available at ScienceDirect

Materials Chemistry and Physics

journal homepage: www.elsevier.com/locate/matchemphys

Towards a new promising dosimetric material from formation of thulium-yttria nanoparticles with EPR response

S.C. Santos *, O. Rodrigues Jr., L.L. Campos

Instituto de Pesquisas Energeticas e Nucleares – IPEN, Av. Prof. Lineu Prestes, 2242, Cidade Universitaria, Sao Paulo, Brazil

HIGHLIGHTS

- Cubic C-type thulium-yttria nanoparticles are formed by a relative low temperature hydrothermal synthesis.
- Thulium-yttria nanoparticles exhibit mean particle size less than 160 nm.
- Doping with thulium improves remarkably EPR response of yttria.
- Thulium-yttria nanoparticles are promising for radiation dosimetry use.

ARTICLE INFO

Keywords:
Yttria
Thulium oxide
Rare earths
EPR
Radiation dosimetry
Ceramic processing

ABSTRACT

Advances toward new materials for dosimetry application is essential to enhance quality assurance and quality improvement practices based on radiation protection concept. Face to this challenge the present work reports an approach to produce thulium-yttria nanoparticles with electron paramagntic resonance response by an alternative hydrothermal synthesis based on a relative low temperature and pressure. Distinct compositions of thulium-yttria nanoparticles with up to 2 at.%Tm (at.%, atomic percentage) were prepared and characterized by XRD, SEM, PCS, and EPR. The proposed synthesis method followed by thermal treatment of the precursor powder at 1100 °C for 2 h provided thulium-yttria nanoparticles with rounded shape, cubic C-type structure, and mean particle size (d_{50}) less than 160 nm. Among all compositions formed, thulium-yttria nanoparticles prepared with 0.1%Tm presented the most remarkable EPR response. The production of fine thulium-yttria nanoparticles with EPR response supply meaningful parameters to advance in the formation of new dosimetry materials based on rare earths.

1. Introduction

Radiation dosimetry provides accuracy and safely in activities in which ionizing radiation is used as energy production [1], industry [2], medicine [3], and food [4]. Highly safe procedures related to radiation detection and dose evaluation to environmental control and personal control demand innovative materials that exhibit suitable response as a function of radiation dose that they are exposed. Even though dysprosium doped calcium sulfate ($CaSO_4$:Dy) presents high effective atomic number (15.3), it is widely used as thermoluminescent dosimeter for diverse types of radiation such as, beta [5], gamma [6], X-ray [7], clinical electron [8], clinical photon [9], UV [10], and laser [11], due to its great reproducibility, high sensitiveness, excellent optical absorbance (OA) properties, and Electron Paramagnetic Resonance (EPR) response, excellent reproducibility and high sensitivity (40 times higher than LiF: Mg,Ti) [12]. Lithium fluoride (LiF) is a standard thermoluminescent (TL) dosimeter, which is routinely used in radiation protection dosimetry [13–16]. Mrozik et al. [17] proposed that dopants (Mg, P, Cu, Ti) may have a significant influence on radio-photoluminescent (RPL) effect on LiF, which indicates that RPL is not entirely driven by intrinsic electron defects as F_2 and F_3^+ centers.

Advances toward new materials for dosimetry application is essential to enhance quality assurance and quality improvement practices based on radiation protection concept [18–20]. The hydrothermal synthesis [21] provides the construction of a material by means of manipulation of atoms and molecules from colloidal suspensions under relative low temperature. The great advantage of hydrothermal synthesis consists in producing particles with controlled chemical stoichiometry. Besides, as

* Corresponding author. Energy and Nuclear Research Institute, 2242 Lineu Prestes Avenue University City, 05508000, São Paulo, Brazil.
E-mail addresses: silas.cardoso@alumni.usp.br (S.C. Santos), rodrijr@ipen.br (O. Rodrigues), lcrodri@ipen.br (L.L. Campos).

https://doi.org/10.1016/j.matchemphys.2020.124005
Received 16 September 2020; Received in revised form 27 October 2020; Accepted 1 November 2020
Available online 9 November 2020
0254-0584/

synthesized particles exhibit narrow particle size distribution, uniform shape, large specific surface area and high relative density (based on theoretical density). Many innovative materials have been produced by this method [22–27]. Chan et al. [28] obtained high aspect ratio wollastonite nanofibers by processing at 200 °C for 16 h. Carregosa et al. [29] reported that CeO_2 powders exhibited high densification at sintering temperatures 300 °C lower than that generally used to obtain dense CeO_2 ceramics. Hu et al. [30] produced W–Y_2O_3 composite nanopowders with mean particle size of 15.1 nm and narrow particle size distribution. In addition, Y_2O_3 alloys presented refined W grains of about 210 nm and relative density of 98.0%.

Rare earths (RE) exhibit great and unique chemical and physical properties, being addressed as critical materials by European Union and United States [31,32]. Belong RE series, yttria (Y_2O_3) has been widely used as host material to receive other REs due to its intrinsic lattice characteristics. Huerta et al. [33]observed that yttria tri-doped powders (4 at.% of Er, 2 at.% of Li and 2 at.% of Yb) exhibited around of 3.5 times more 950–1090 nm emissions in comparison with Yb^{3+} free samples. Wang et al. [34] reported that the luminescence response of yttria nanopowders was improved remarkably by doping with 2 at% of Nd. Kruk et al. [35] revealed that the transparency of yttria sinters ca be reduced to about 30% by doping with lanthanium. Gan et al. [36] obtained highly transparent Nd-doped yttria ceramics with transmittance of 74.3% at 400 nm and 81.3% at 1100 nm, using 1 at.% ZrO_2 and 3 at.% La_2O_3 as sintering aids, followed by hot pressing at 1600 °C for 3 h.

The present paper reports an approach to obtain thulium-yttria nanoparticles with controlled powder characteristics and EPR reponse by an alternative hydrothermal synthesis performed in relative low temperature and pressure. The as synthesized powders represent an innovative approach toward new dosimetric materials based on rare earth oxides.

2. Experimental

Thulium yttria powders (Y_2O_3:Tm) with controlled characteristics such as stoichiometry, shape, size, and density were synthesized using the following starting materials: yttria (Y_2O_3, 99.99%, Alfa Aesar GmbH), thulium oxide (Tm_2O_3, 99.999%, Alfa Aesar GmbH), nitric acid (HNO_3, Synth), ammonium hydroxide (NH_4OH, Casa Americana).

A facile hydrothermal process [38] was performed to synthesize Y_2O_3:Tm powders, with thulium content varying from 0.1 up to 2.0 at% (at.%, atomic percentage). All powder compositions were determinated by stoichiometry calculations, having yttria and thulium oxide as references. The precursor powders were obtained from a stock solution processed at 60 °C for 6 h into a condenser system.

Thermal decomposition assay of the precursor powders was performed in order to provide a controlled thermal treatment to obtain crystalline Y_2O_3:Tm powders. A sample of 5 mg was heated from 25 °C up to 1400 °C in air atmosphere (Lindberg Blue, Haake), in which its mass was measured in each 100 °C, using an analytical balance (Mettler Toledo, AB204-S). In order to avoid any moisture absorption, the sample was not fully cooled down until environmental temperature, but at 50 °C. Therefore, the sample heaviness was measured while it was still heated. Afterwards, the sample was put back into the furnace to continue the thermal evaluation.

The first derivative of mass loss curve as a function of temperature was calculated in order to determine in which temperature the maximum decomposition peak of sample takes place.

As synthesized Y_2O_3:Tm powders were characterized as follows: mean particle size (d_{50}) by Photon Correlation Spectroscopy (PCS, Litesizer500, Anton Paars), using hydrodynamic diameter model [40] as shown in (Eq. (1)); X-ray diffraction (XRD, Rigaku Multiflex, Japan), with an angular range (2θ) from 15 to 70°, scanning of 0.5°.min^{-1} and Kα source, in which crystallite size was calculate by Scherrer model [41] (Eq. (2)), and based on the measurement of full-width at half-maximum (FWHM) values in the corresponding XRD pattern; helium pycnometric

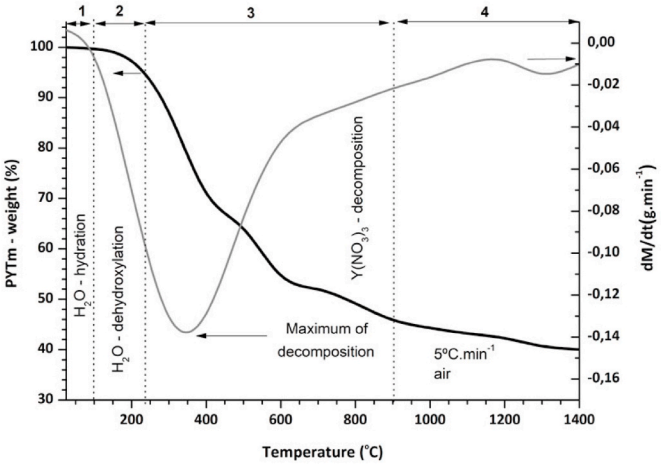

Fig. 1. Thermal decomposition of thulium-yttria precursor up to 1400 °C in air atmosphere during a heating rate of 5 °C.min^{-1}. Black curve illustrates the mass loss; light grey curve illustrates the first derivative of the mass loss curve and the temperature in which the decomposition is maximum.

(Pycnometer Micrometrics 1330), and Scanning Electron Microscopy (SEM, INCAx-act, Oxford Instruments).

$$d_{50} = \left(\frac{K_{BT}}{3\pi\eta(T)D_t}\right)\cdot[\text{nm}] \quad (1)$$

Where, K_{BT} is Boltzmann constant ($1.38064852.10^{-23}\ m^2\ kg.\ s^{-2}.K^{-1}$), T is temperature (K), η(T) is viscosity of the suspending liquid and, D_t is particle diffusion coefficient.

$$dc = \left(\frac{0.9\lambda}{\beta cos\theta}\right)\cdot[\text{nm}] \quad (2)$$

Paramagnetic response of Y_2O_3:Tm powders as a function of dopant concentration (Tm^{3+}) was evaluated by electron paramagnetic resonance using a X-band EPR spectrometer (Bruker EMX PLUS), under room temperature and atmosphere. EPR spectra of samples were recorded in field modulation frequency of 100 kHz, microwave power of 2.5 mW, center field of 300 mT, sweep width of 300 mT, modulation amplitude of 0.4 mT, time constant of 0.01 ms, 10 scans, temperature of 20 °C, environmental atmosphere, under controlled humidity, and using DPPH (2, 2-Diphenyl-1-picrylhydrazyl, Bruker) as EPR reference.

3. Results and discussion

Synthesis method provides conditions to form advanced materials through manipulation of a fraction of atoms and molecules. As a result, new materials with suitable properties and characteristics can be produced for high advanced applications as radiation dosimetry. The thermal decomposition behaviour of thulium-yttria precursor (PYTm) treated up to 1400 °C is illustrated in Fig. 1. The bold curve represents residual mass as a function of temperature and time, in which four different events were observed. The first one is observed from 25 to 100 °C, which is due to broken down of weak bonded water molecules (hydration), and resulting in residual mass around of 1%. The second event takes place in temperature range between 100 and 245 °C as a result of breaking strong bonded water molecules (dehydration) and residual mass of 9%. The third event occurs in temperature range from 245 to 900 °C, in which decomposition of yttrium nitrate - $Y(NO_3)_3$ occur, resulting in mass loss around of 50%. It suggest that formation of crystalline thulium-yttria powders may be occurred. Over this temperature, thermal decomposition goes on up to the temperature limit of 1400 °C, resulting in loss mass of 10%. Considering the four events described, the precursor exhibited total loss mass of 58%.

The sharp curve (Fig. 1) is based on the first derivative of the bold

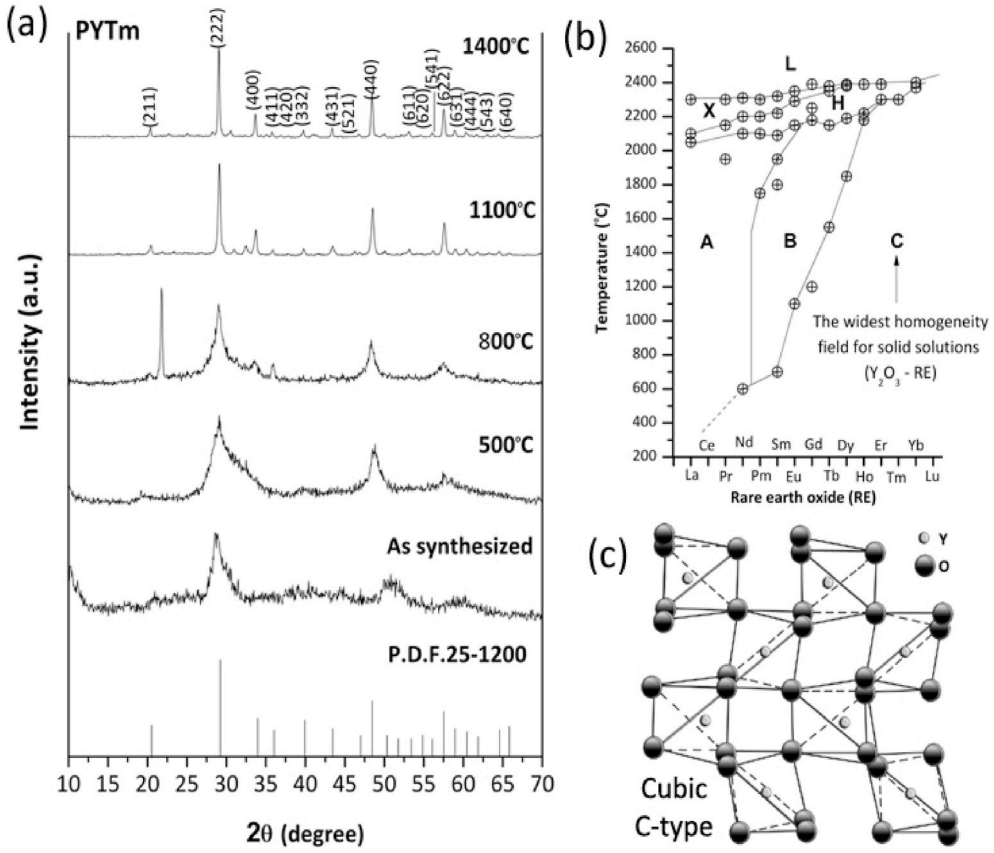

Fig. 2. Formation of crystalline thulium-yttria powders: (a) XRD curves; (b) polymorphic diagram of rare earth oxides [37]; and (c) cubic C-type structure that is usually formed by powder synthesis.

curve, and shows the temperature in which the maximum decomposition of each substance that composes a sample takes place. For PYTm, yttrium nitrate exhibited maximum decomposition peak at 350 °C, with mass loss of 20%. Face to the results presented in Fig. 1, to form crystalline thulium-yttria powders three thermal treatment essays with heating rate of 10C.min^{-1} and step of 2 h were proposed as following: 800, 1000 and 1100 °C.

X-ray diffraction curves of PYTm treated up to 1400 °C in room atmosphere are illustrated in Fig. 2a. The as sythesized samples exhibited amorphous spectra and a short range peak recorded at 29.5° (2Θ). Possibly, in this condition there are crystallites whose dimensions are very hard to indentify by XRD. For samples treated in a temperature range between 500 and 800 °C, it is observed the initial formation of diffraction planes recorded at 29.5° and 50°. In addition, it is seen that samples treated at 1100 °C exhibited cubic C-type structure, corresponding to Powder Diffraction File (JCPDS. 25–1200), with the main diffraction peaks recorded as follows: 29.5° (222); 53.0° (440), and 57.6° (622).

All rare earth oxides (RE_2O_3) can exhibit cubic C-type form as illustrated by transition phase diagram [37] in Fig. 2b. According to this diagram, five polymorphic forms designated as A, B, C, X, and H can be formed. The forms A, B, and C can be formed below 2000 °C, whereas X and H can be established above this temperature. In addition, above 2400 °C RE_2O_3 are in liquid form. Moreover, type C presents the broadest range of stability among all forms. The polymorphic forms and transition temperatures (approximation) of some RE_2O_3 are as following: Dy_2O_3 (C-type 2000 °C → B-type 2200 °C → H-type); Eu_2O_3 (C-type 1000 °C → B-type 2100 °C → H-type 2340 °C → X-type); and Tm_2O_3 (C-type 2300 °C → H-type).

Yttria which belongs to the rare earth group can exhibit one of the following crystalline structures: monoclinic (A-type), hexagonal (B-type), and cubic (C-type). As illustrated in Fig. 2b, cubic C-type is the most common form of yttria, being stable even in high temperature range (800 °C < T < 2400 °C). Besides, yttria presents wide homogeneity field to form C-type solid solutions with other RE elements as Eu, Sm, Gd, Dy, Er, and Tm. Nevertheless, some investigations [38–40] revealed that yttria can present polymorphism under high temperature and pressure.

The ball model of cubic C-type yttria is illustrated in Fig. 2c. Yttria exhibits crystal lattice features that enable the insertion of rare earth ions as (Dy^{3+} [41], Tm^{3+} [42], Yb^{3+} [43], Tb^{3+} [44], $Ce^{2,3+}$ [45]) into its structure. This insertion refers to the term doping and is concerned to enhance yttria characteristics as luminescence and paramagnetism. Doping Y_2O_3 with Tm^{3+} gives rise to substitution of Y^{3+} to Tm^{3+} in C_2 and S_6 sites without substantial distortion of crystal lattice, seeing that ytrrium and thulium exhibits similar crystal lattice and ionic radious (r_Y = 0.092 nm [46]; r_{Tm} = 0.095 nm [47]).

On Fig. 2c, it is reported [48] that the luminescence response of yttria is associated with symmetry axis wherein RE ion is located. As RE ion is located at C3i, S6 summetry axes, low luminescence response is produced due to low probability of electron transitions. On the other hand, as RE ion fill C_2 symmetry, transitions $^5D_0$ - $^7F_2$ are provided and as consequence, luminescence response is intensified [49].

The process to form crystalline yttria varies on raw materials nature, synthesis route, and thermal treatment. The thermal energy induces transition from amorphous to crystalline state of powders and changes on characteristics as size and shape. Zhang et al. [8] produced micro particles of europium-yttria by hidrothermal method, followed by thermal treatment at 800 °C for 5 h in environmental atmosphere. Shivaramu et al. [38] obtained nanoparticles of yttria by combustion synthesis and thermal treatment at 600 °C for 2 h. Lojpur et at [39]. synthesized terbium-yttria powders with accicular morphology by

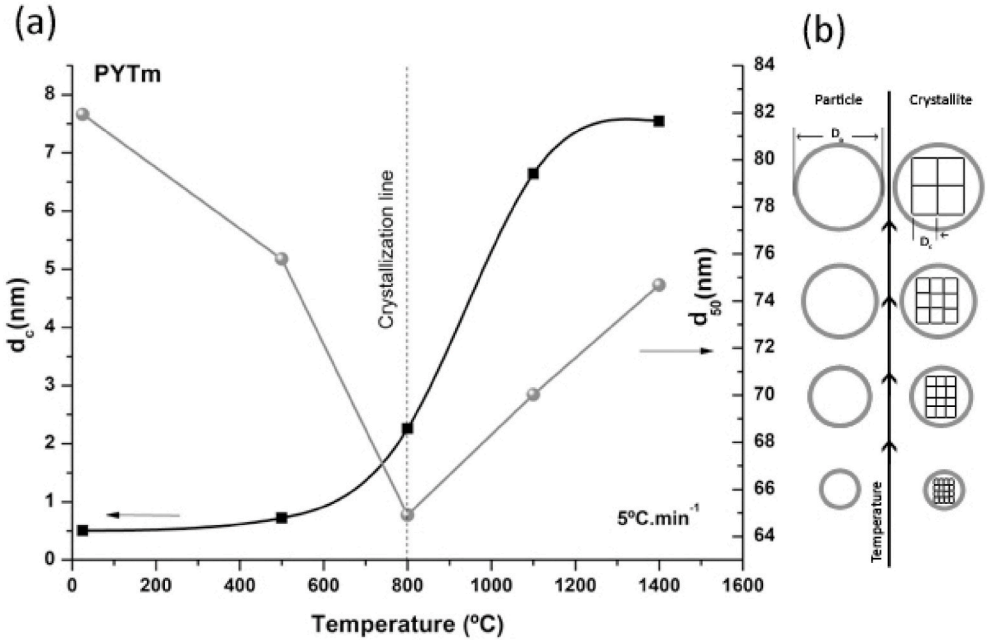

Fig. 3. (a) Correlation between crystallite size (d_c) and mean particle size (d_{50}) of thulium-yttria precursor during thermal treatment up to 1400 °C; (b) representation about increase of d_c and d_{50} as a function of temperature.

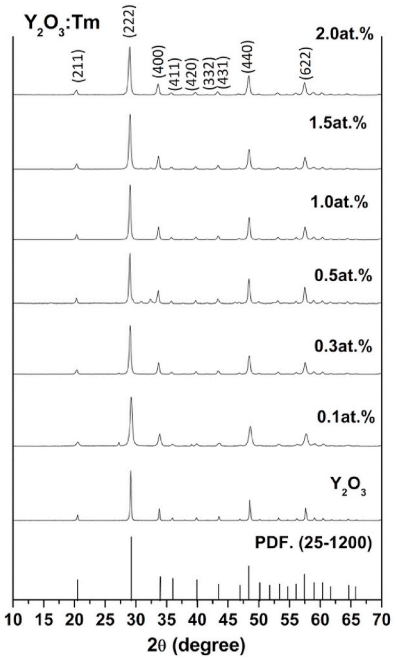

Fig. 4. XRD curves of Y_2O_3:Tm powders synthesized by hydrothermal synthesis, followed by thermal treatment at 1100 °C for 2 h in room atmosphere.

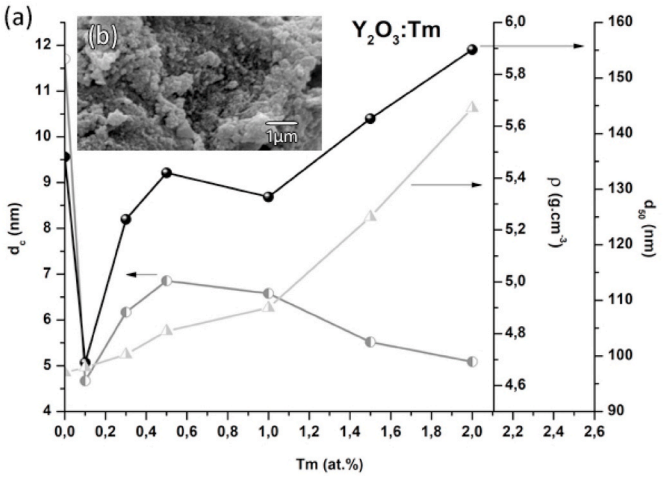

Fig. 5. Thulium-yttria powder characteristics: (a) curves of crystallite size (d_c), pycnometric density (ρ), and mean particle size (d_{50}); (b) SEM image of composition prepared with 0.5 at.%Tm.

powder mixture and thermal treatment at 1100 °C for 1 h.

Thermal treatment usually provides increasing in particle size due to formation of larger aggregates. In Fig. 3 is illustrated a correlation between particle size and crystallite size of precursor powder as a function of temperature used during thermal treatment. As synthesized powders were constituted of fine particles, whose mean diameter size around of 64 nm and crystallite size of 7.5 nm. Moreover, the thermal treatment performed in this study to form thulium-yttria powders was successful to provide particles with nanosized distribution, in which small difference of 20 nm in diameter size and 7 nm of crystallite size of samples treated from 800 °C to 1400 °C were observed.

XRD curves of thulium-yttria powders with up to 2 at.%Tm are shown in Fig. 4. As illustrated in Fig. 2c yttria exhibits Y^{3+} ions in C_2 and C_{3i},S_6 in the presence of six oxygen atoms. Since yttrium and thulium present similar ionic radius, doping is characterized as substitutional and no lattice distortion is induced. In addition, Tm^{3+} ions tend to occupy C_2 and C_{3i},S_6 positions to form energy levels. Based on results shown in Fig. 4, the hydrothermal method performed followed by thermal treatment proposed was successful to form thulium-yttria powders with cubic C-type structure, without secondary phases within (2Θ) 10–70°, according to JCPDS 25–1200.

Particle characteristics of thulium-ytrria powders with distint compositions formed at 1000 °C for 2 h are shown in Fig. 5a. Particle size variation is represented by the black line and revealed that thulium concentration increased directly particle size from 50 to 150 nm in addition, picnometric density increased significantly from 4.7 (“pure

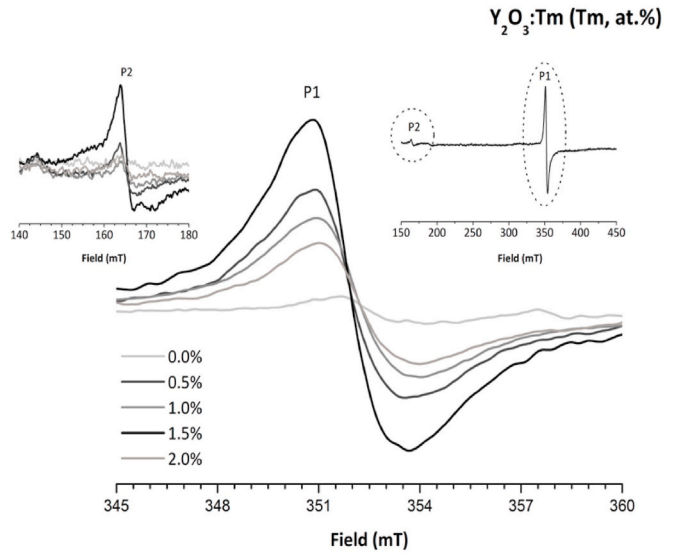

Fig. 6. EPR curves of as synthesized powders of thulium-yttria recorded in environmental temperature.

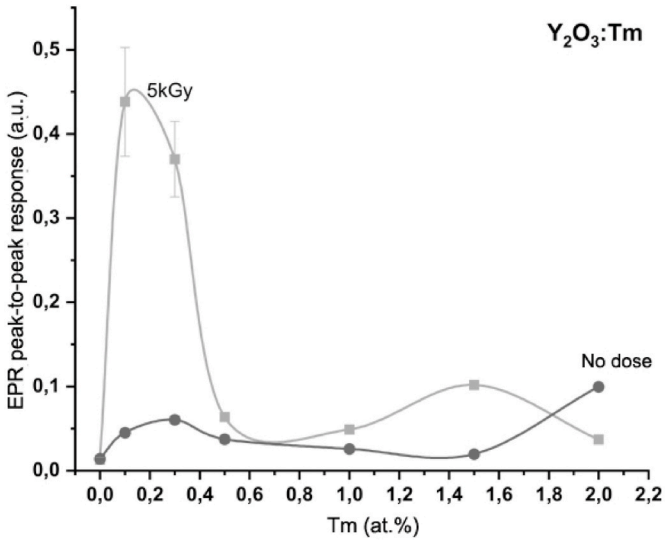

Fig. 7. EPR peak-to-peak high curves of thulium-yttria powders as a function of Tm concentration and dose.

yttria") to 5.9 g cm^{-3} (Y_2O_3:Tm, 2 at.%). On the other hand, crystallite size (d_c) exhibited a small variation (between 5 and 7 nm), which confirms the substitutional characteristic of doping. Moreover, SEM image illustrated in Fig. 5b revealed that thulium-yttria powders (0.5 at%Tm) are constituted by fine particles, with accicular morphology and size inferior than 1 μm. The control of particle characteristics contributes to improve particle packing during shaping process. In addition, powder compacts formed from particles with controlled characteristics after sintering often provide ceramic bodies with dense microstructure, homogeneous phase, free of visible defects, and suitable response for end-use.

Particle morphology is an important feature in many advanced applications. Vatankhah et al. [50] during seeded emulsion polymerization study, found out that particles with spherical morphology presented better drug release than cauliflower-like ones. Xiu et al. [51] reported that particle circularity exerts the greatest influence on powder flowability of microcrystalline cellulose. Limousin et al. [52] observed that the morphology of the hybrid latex particles directly influences the final film morphology, in which hemispherical particles provide aggregated hard domains and higher strength. Wei et al. [53] reported that rough particulates in concrete can increase stress bearing capacity by enhancing intra-aggregate fracture paths. In our recent work [54], micro ceramic rods with dense microstructure were produced by bio-prototyping from europium-yttria nanoparticles with accicular shape.

Processing procedures as comminution, grinding, seiving, as well as radiation provide the development of unpaired electrons in materials. The Electron Paramagnetic Resonance (EPR) is a non destructive and non intrusive technique that provides structural information from chemical and physical processes by detection of unpaired electrons. Thus, EPR is a useful technique to advance in development of rare earth based dosimetry materials.

In Fig. 6 are illustrated EPR spectra of thulium-yttria compositions containing up to 2 at.%Tm. Apart from 0.5 at%Tm it is seen that EPR spectra exhibited additional resonance peak (p_2) as indicative of Tm^+ recorded at 164.0 mT and g 2.0065. The main peak (p_1) was recorded at 350 mT, with width of 3 mT and g 2.0040. Considering yttria spectra, it is observed that a shift around of 0.0040. On p_2 peak, the shift was around of 0.0050 g. In addition, p_1 peak exhibited significant increase for composition 1.5 at%Tm compared to "pure" yttria. Based on results, doping yttria with thulium enhances EPR response of samples due to formation of new defects, as well as energy transfer from Tm^{3+} ion to yttria host.

The process of doping yttria with thulium consists in increasing EPR response of yttria as a function of radiation dose. In Fig. 7 are presented EPR response curves of as synthesized powders and irradiated ones with 5 kGy. For as synthesized samples it is seen that 2 at%Tm exhibited the highest EPR response. On the other hand, powders irradiated with 5 kGy presented great improvement of EPR response for samples with 0.1 e 0.3%at Tm. The insertion of low concentrations of Tm provided substantial formation of crystal defects, which in turn can trap more unpaired electrons formed during irradiation process. In addition, the solid state features of yttria rely on its symmetry axis wherein RE ion is located. As RE ion is located at C_{3i}, S_6 summetry axes, low EPR response is produced due to low probability of electron transitions. On the other hand, as RE ion fill C_2 symmetry, more electron transitions are provided and as consequence, EPR response is intensified. Based on results, doping with 0.1%at Tm was more effective in promoting new electron defects and provided the highest EPR response.

Thulium-yttria particles exhibits significant EPR response, an evidence that indicates this ceramic material as a promising candidate for radiation dosimetry. Nevertheless, additional studies have to be done in order to confirm these evidences and to present this material as an alternative for those widely used as dysprosium doped calcium sulfate. With the aim to provide more findings and innovative results, a new study on thulium-yttria micro rods is under development.

4. Conclusion

Cubic C-type thulium-yttria nanoparticles with rounded shape, mean particle size less than 160 nm, and electron paramagnetic resonance (EPR) response were obtained by an alternative hydrothermal synthesis performed at 60 °C for 6 h in relative low pressure, followed by thermal treatment at 1100 °C for 2 h in environmental atmosphere. Thulium-yttria nanoparticles prepared with 0.1 at.%Tm exhibited the most remarkable EPR response as a function of dose among all compositions. The proposed synthesis was effective to produce nanoparticles with suitable characteristics for colloidal processing toward new dosimetry materials.

CRediT authorship contribution statement

S.C. Santos: Conceptualization, Methodology, Validation, Formal analysis, Investigation, Writing - original draft, Writing - review &

editing, Visualization, Preparation, creation and/or presentation of the published work, Visualization, data presentation. **O. Rodrigues:** Validation, Resources, Data curation, Supervision, Project administration. **L. L. Campos:** Validation, Resources, Data curation, Supervision, Project administration, Funding acquisition.

Declaration of competing interest

The authors declare that they have no known competing financial interests or personal relationships that could have appeared to influence the work reported in this paper.

Acknowledgements

We authors are deeply grateful to Dra. Maria Elisa Chuery Martins Rostelato from Radiation Technology Centre (CTR) localized at Nuclear and Energy Research Institute (IPEN/CNEN-SP, Sao Paulo, Brazil) that kindly allowed us to use particle size analyzer, and MSc. Beatriz Ribeiro Nogueira from the same centre that helped me during my first time in using the equipment. In addition to the following sponsor organizations: São Paulo Research Foundation (FAPESP); National Council for Scientific and Technological Developmen (CNPq); and Coordination for Improvement of High Degree People (CAPES).

References

[1] K. Saidi, A. Omri, Reducing CO2 emissions in OECD countries: do renewable and nuclear energy matter? Prog. Nucl. Energy 126 (2020) 103425, https://doi.org/10.1016/j.pnucene.2020.103425.

[2] M.F. Attallah, H.M. Abdelbary, E.A. Elsofany, Y.T. Mohamed, M.M. Abo-Aly, Radiation safety and environmental impact assessment of sludge TENORM waste produced from petroleum industry in Egypt, Process Saf. Environ. Protect. 142 (2020) 308–316, https://doi.org/10.1016/j.psep.2020.06.012.

[3] J. Abi Jaoude, R. Kouzy, N.D. Nguyen, D. Lin, S.S. Noticewala, E.B. Ludmir, C. M. Taniguchi, Radiation therapy for patients with locally advanced pancreatic cancer: evolving techniques and treatment strategies, Curr. Probl. Canc. (2020) 100607, https://doi.org/10.1016/j.currproblcancer.2020.100607.

[4] R.G. Moreira, M.E. Castell-Perez, 2.01 - Fundamentals of Food Irradiation, Knoerzer K., Muthukumarappan K.B.T.-I.F.P.T. (Eds.), Elsevier, Oxford, 2021, pp. 1–18, https://doi.org/10.1016/B978-0-12-815781-7.00008-1.

[5] A.M.B. Silva, D.O. Junot, L.V.E. Caldas, D.N. Souza, Structural, optical and dosimetric characterization of CaSO4:Tb, CaSO4:Tb, Ag and CaSO4:Tb,Ag(NP), J. Lumin. 224 (2020) 117286, https://doi.org/10.1016/j.jlumin.2020.117286.

[6] L.A. Forner, C. Viccari, P. Nicolucci, Dosimetric properties of thermoluminescent pellets of CaSO4 doped with rare earths at low doses, Radiat. Phys. Chem. 171 (2020) 108704, https://doi.org/10.1016/j.radphyschem.2020.108704.

[7] R.G. Nair, K. Madhukumar, C.M.K. Nair, S. Jayasudha, V.M. Anandakumar, T. S. Elias, M. Komath, Thermoluminescence studies of CaSO4:Dy,P,Si phosphor under X-ray irradiation, Ceram. Int. 44 (2018) 3492–3496, https://doi.org/10.1016/j.ceramint.2017.11.086.

[8] S.B. Almeida, D. Villani, R.K. Sakuraba, A.C.P. Rezende, L.L. Campos, Comparative study of the TL response of LiF:Mg,Ti and CaSO4:Dy in the clinical electron beams dosimetry applied to total skin irradiation (TSEB) treatments, Radiat. Phys. Chem. 155 (2019) 121–126, https://doi.org/10.1016/j.radphyschem.2018.05.025.

[9] F.D.G. Rocha, D. Villani, V.P. Campos, M.S. Nogueira, M.E. Goulart, V.A. Sichito, L. L. Campos, Performance of TL and OSL techniques using CaSO4 and Al2O3 dosimeters for mean glandular dose (MGD) and entrance surface skin dose (ESD) determination in a digital mammographic unit as alternative dosimeters, Radiat, Phys. Chem. 155 (2019) 48–52, https://doi.org/10.1016/j.radphyschem.2018.06.037.

[10] N.T. Mandlik, S.R. Rondiya, N.Y. Dzade, M.S. Kulkarni, P.D. Sahare, B.C. Bhatt, S. D. Dhole, Thermoluminescence, photoluminescence and optically stimulated luminescence characteristics of CaSO4:Eu phosphor: experimental and density functional theory (DFT) investigations, J. Lumin. 221 (2020) 117051, https://doi.org/10.1016/j.jlumin.2020.117051.

[11] S. Chaurasia, M. Kumar, A.K. Poswal, D.S. Munda, L.J. Dhareshwar, R.K. Kher, G. Chourasiya, Comparison of thermo-luminescent detectors and X-ray vacuum detectors for measurement of X-ray yield from gold plasma produced by a sub-nanosecond Nd:glass laser, Nucl. Instruments Methods Phys. Res. Sect. a-Accelerators Spectrometers Detect. Assoc. Equip. 595 (2008) 395–400.

[12] A. Piaskowska, B. Marczewska, P. Bilski, A. Mandowski, E. Mandowska, Photoluminescence measurements of LiF TL detectors, Radiat. Meas. 56 (2013) 209–212.

[13] B. Obryk, H.J. Khoury, V.S. de Barros, P.L. Guzzo, P. Bilski, On LiF:Mg,Cu,P and LiF:Mg,Ti phosphors high & ultra-high dose features, Radiat. Meas. 71 (2014) 25–30, https://doi.org/10.1016/j.radmeas.2014.02.002.

[14] A. Parisi, J. Dabin, W. Schoonjans, O. Van Hoey, P. Mégret, F. Vanhavere, Photon energy response of LiF:Mg,Ti (MTS) and LiF:Mg,Cu,P (MCP) thermoluminescent detectors: experimental measurements and microdosimetric modeling, Radiat. Phys. Chem. 163 (2019) 67–73, https://doi.org/10.1016/j.radphyschem.2019.05.021.

[15] A. Parisi, P. Olko, J. Swakoń, T. Horwacik, H. Jabłoński, L. Malinowski, T. Nowak, L. Struelens, F. Vanhavere, Mitigation of the proton-induced low temperature anomaly of LiF:Mg,Cu,P detectors using a post-irradiation pre-readout thermal protocol, Radiat. Meas. 132 (2020) 106233, https://doi.org/10.1016/j.radmeas.2019.106233.

[16] D. Sorger, H. Stadtmann, W. Sprengel, Fading study and readout optimization for routinely use of LiF:Mg,Ti thermoluminescent detectors for personal dosimetry, Radiat. Meas. 135 (2020) 106342, https://doi.org/10.1016/j.radmeas.2020.106342.

[17] A. Mrozik, P. Bilski, B. Marczewska, B. Obryk, K. Hodyr, W. Gieszczyk, Radio-photoluminescence of highly irradiated Lif:Mg,Ti and Lif:Mg,Cu,P detectors, Radiat. Meas. 71 (2014) 31–35, https://doi.org/10.1016/j.radmeas.2014.05.013.

[18] Occupational Radiation Protection, International atomic energy agency, Vienna, https://www.iaea.org/publications/11113/occupational-radiation-protection, 2018.

[19] Radiation Protection of the Public and the Environment, International atomic energy agency, Vienna, https://www.iaea.org/publications/11183/radiation-protection-of-the-public-and-the-environment, 2018.

[20] Radiation Protection and Safety of Radiation Sources, International Basic Safety Standards, INTERNATIONAL ATOMIC ENERGY AGENCY, Vienna, 2014. https://www.iaea.org/publications/8930/radiation-protection-and-safety-of-radiation-sources-international-basic-safety-standards.

[21] E. Suvaci, E. Özel, Hydrothermal Synthesis, Ref. Modul. Mater. Sci. Mater. Eng. (2020), https://doi.org/10.1016/B978-0-12-803581-8.12096-X.

[22] M.S. Medina, J.C. Bernardi, A. Zenatti, M.T. Escote, A new approach to obtain calcium cobalt oxide by microwave-assisted hydrothermal synthesis, Ceram. Int. 46 (2020) 1596–1600, https://doi.org/10.1016/j.ceramint.2019.09.130.

[23] X. Yu, Z. Han, H. Tang, J. Xie, X. Mi, Investigating luminescence properties and energy transfer of Ca3(PO4)2: Dy3+/Eu3+ phosphor via hydrothermal synthesis, Opt. Mater. 106 (2020) 110009, https://doi.org/10.1016/j.optmat.2020.110009.

[24] S.H. Daryan, A. Khavandi, J. Javadpour, Surface engineered hollow hydroxyapatite microspheres: hydrothermal synthesis and growth mechanisms, Solid State Sci. 106 (2020) 106301, https://doi.org/10.1016/j.solidstatesciences.2020.106301.

[25] M.L. Hancock, R.A. Yokel, M.J. Beck, J.L. Calahan, T.W. Jarrells, E.J. Munson, G. A. Olaniyan, E.A. Grulke, The characterization of purified citrate-coated cerium oxide nanoparticles prepared via hydrothermal synthesis, Appl. Surf. Sci. 535 (2021) 147681, https://doi.org/10.1016/j.apsusc.2020.147681.

[26] H. Wu, X. Pang, J. Bi, L. Wang, Z. Li, L. Guo, H. Liu, Q. Meng, H. Jiang, C. Liu, L. Wang, Cellulose nanofiber assisted hydrothermal synthesis of Ni-rich cathode materials with high binding particles for lithium-ion batteries, J. Alloys Compd. 829 (2020) 154571, https://doi.org/10.1016/j.jallcom.2020.154571.

[27] N.J. Ismail, M.H.D. Othman, S. Abu Bakar, S.H. Sheikh Abdul Kadir, M.H. Abd Aziz, M.A.B. Pauzan, S.K. Hubadillah, T. El-badawy, J. Jaafar, M.A. Rahman, Hydrothermal synthesis of TiO2 nanoflower deposited on bauxite hollow fibre membrane for boosting photocatalysis of bisphenol A, J. Water Process Eng. 37 (2020) 101504, https://doi.org/10.1016/j.jwpe.2020.101504.

[28] J.X. Chan, J.F. Wong, A. Hassan, N.K. Shrivastava, Z. Mohamad, N. Othman, Green hydrothermal synthesis of high aspect ratio wollastonite nanofibers: effects of reaction medium, temperature and time, Ceram. Int. 46 (2020) 22624–22634, https://doi.org/10.1016/j.ceramint.2020.06.025.

[29] J.D.C. Carregosa, J.P.F. Grilo, G.S. Godoi, D.A. Macedo, R.M. Nascimento, R.M.P. B. Oliveira, Microwave-assisted hydrothermal synthesis of ceria (CeO2): microstructure, sinterability and electrical properties, Ceram. Int. 46 (2020) 23271–23275, https://doi.org/10.1016/j.ceramint.2020.06.021.

[30] W. Hu, Z. Dong, Z. Ma, Y. Liu, W–Y2O3 composite nanopowders prepared by hydrothermal synthesis method: Co-deposition mechanism and low temperature sintering characteristics, J. Alloys Compd. 821 (2020) 153461, https://doi.org/10.1016/j.jallcom.2019.153461.

[31] U.S.G.S. Department of the Interior, A Federal Strategy to Ensure Secure and Reliable Supplies of Critical Minerals, U.S.G.S. Department of the Interior, U.S.G.S. Department of the Interior, United States, 2018. https://www.usgs.gov/news/interior-releases-2018-s-final-list-35-minerals-deemed-critical-us-national-security-and.

[32] T.E. Union, O. of the E. Union, Report on Critical Raw Materials and the Circular Economy, The European Union, 2018, https://doi.org/10.2873/167813.

[33] E.F. Huerta, J. De Anda, I. Martínez-Merlin, U. Caldiño, C. Falcony, Near-infrared luminescence spectroscopy in yttrium oxide phosphor activated with Er3+, Li+ and Yb3+ ions for application in photovoltaic systems, J. Lumin. 224 (2020) 117271, https://doi.org/10.1016/j.jlumin.2020.117271.

[34] N.L. Wang, X.Y. Zhang, Z.H. Bai, Synthesis of neodymium doped yttria nanopowders by microwave-assisted glycine combustion method and the powder characteristics, Ceram. Int. 40 (2014) 4903–4908, https://doi.org/10.1016/j.ceramint.2013.10.073.

[35] A. Kruk, A. Wajler, M. Bobruk, A. Adamczyk, M. Mrózek, W. Gawlik, T. Brylewski, Preparation of yttria powders co-doped with Nd3+, and La3+ using EDTA gel processes for application in transparent ceramics, J. Eur. Ceram. Soc. 37 (2017) 4129–4140, https://doi.org/10.1016/j.jeurceramsoc.2017.05.040.

[36] L. Gan, Y.-J. Park, L.-L. Zhu, H.-N. Kim, J.-W. Ko, J.-W. Lee, Highly transparent Nd-doped yttria ceramics fabricated by hot pressing with ZrO2 and La2O3 as sintering additives, J. Alloys Compd. 763 (2018) 192–198, https://doi.org/10.1016/j.jallcom.2018.05.304.

[37] J.P. Coutures, R. Verges, M. Foex, Comparison of solidification temperatures of different rare earth sesquioxides; effect of atmosphere, Rev. Int. Des Hautes Temp.

Des Refract. 12 (1975) 181–185. http://inis.iaea.org/search/search.aspx?orig_q=RN:07227877.

[38] K. Riener, N. Albrecht, S. Ziegelmeier, R. Ramakrishnan, L. Haferkamp, A. B. Spierings, G.J. Leichtfried, Influence of particle size distribution and morphology on the properties of the powder feedstock as well as of AlSi10Mg parts produced by laser powder bed fusion (LPBF), Addit. Manuf. 34 (2020) 101286, https://doi.org/10.1016/j.addma.2020.101286.

[39] X. Qin, Y. Ju, S. Bernhard, N. Yao, Flame synthesis of Y 2 O 3 :Eu nanophosphors using ethanol as precursor solvents, J. Mater. Res. 20 (2005) 2960–2968, https://doi.org/10.1557/JMR.2005.0364.

[40] H. Starr, Territory, proximity, and spatiality: the geography of international conflict, Int. Stud. Rev. 7 (2005) 387–406, https://doi.org/10.1111/j.1551-2916.2005.00506.x.

[41] T. Verma, S. Agrawal, Optical studies and estimation of kinetic parameters for dysprosium activated yttrium oxide phosphors, Optik 160 (2018) 361–370, https://doi.org/10.1016/j.ijleo.2018.02.015.

[42] A. Sidorowicz, A. Wajler, H. Węglarz, M. Nakielska, K. Orliński, R. Diduszko, A. Olszyna, Preparation and characterization of thulium doped yttrium oxide (Tm: Y2O3) powders, J. Alloys Compd. 709 (2017) 293–298, https://doi.org/10.1016/j.jallcom.2017.03.165.

[43] L. Mariscal-Becerra, V.M. Velázquez-Aguilar, M.C. Flores-Jiménez, J. M. Hernández-Álcantara, E. Camarillo-García, C.J. Villagómez, R. Váquez-Arreguín, I. Martínez-Merlin, C. Falcony-Guajardo, H. Murrieta S, Up-conversion luminescence of hafnium, erbium, ytterbium and lithium co-doped yttrium oxide, Opt. Mater. 105 (2020) 109923, https://doi.org/10.1016/j.optmat.2020.109923.

[44] E.-J. Popovici, M. Nazarov, L. Muresan, D.Y. Noh, L.B. Tudoran, E. Bica, E. Indrea, Synthesis and characterisation of terbium activated yttrium tantalate phosphor, J. Alloys Compd. 497 (2010) 201–209, https://doi.org/10.1016/j.jallcom.2010.03.010.

[45] H.K. Jung, C.H. Kim, A.-R. Hong, S.H. Lee, T.C. Kim, H.S. Jang, D.H. Kim, Luminescent and magnetic properties of cerium-doped yttrium aluminum garnet and yttrium iron garnet composites, Ceram. Int. 45 (2019) 9846–9851, https://doi.org/10.1016/j.ceramint.2019.02.023.

[46] A. V Shevchenko, L.M. Lopato, I.E. Kir'yakova, The reactions of HfO2 with Y2O3, Ho2O3, Er2O3, Tm2 O3, Yb2O3 and Lu2O3 at high temperatures, Izv. Akad. Nauk. SSSR - Neorganicheskiye Mater. 20 (1984) 1991–1996.

[47] E.R. Andrievskaya, L.M. Lopato, A. V Shevchenko, V.P. Smirnov, Phase interaction in the system HfO2–Eu2O3, Izv. RAN Neorg. Mater. 33 (1997) 835–838.

[48] E. Zych, M. Karbowiak, K. Domagala, S. Hubert, Analysis of Eu3+ emission from different sites in Lu2O3, J. Alloys Compd. 341 (2002) 381–384. https://doi.org/10.1016/S0925-8388(02)00042-7.

[49] A. Konrad, T. Fries, A. Gahn, F. Kummer, U. Herr, R. Tidecks, K. Samwer, Chemical vapor synthesis and luminescence properties of nanocrystalline cubic Y2O3 : Eu, J. Appl. Phys. 86 (1999) 3129–3133, https://doi.org/10.1063/1.371177.

[50] Z. Vatankhah, E. Dehghani, M. Salami-Kalajahi, H. Roghani-Mamaqani, Seed's morphology-induced core-shell composite particles by seeded emulsion polymerization for drug delivery, Colloids Surf. B Biointerfaces 191 (2020) 111008, https://doi.org/10.1016/j.colsurfb.2020.111008.

[51] H. Xiu, F. Ma, J. Li, X. Zhao, L. Liu, P. Feng, X. Yang, X. Zhang, E. Kozliak, Y. Ji, Using fractal dimension and shape factors to characterize the microcrystalline cellulose (MCC) particle morphology and powder flowability, Powder Technol. 364 (2020) 241–250, https://doi.org/10.1016/j.powtec.2020.01.045.

[52] E. Limousin, N. Ballard, J.M. Asua, The influence of particle morphology on the structure and mechanical properties of films cast from hybrid latexes, Prog. Org. Coating 129 (2019) 69–76, https://doi.org/10.1016/j.porgcoat.2019.01.015.

[53] D. Wei, R.C. Hurley, L.H. Poh, D. Dias-da-Costa, Y. Gan, The role of particle morphology on concrete fracture behaviour: a meso-scale modelling approach, Cement Concr. Res. 134 (2020) 106096, https://doi.org/10.1016/j.cemconres.2020.106096.

[54] S.C. Santos, O. Rodrigues, L.L. Campos, Bio-prototyping of europium-yttria based rods for radiation dosimetry, Mater. Chem. Phys. (2017), https://doi.org/10.1016/j.matchemphys.2017.07.063.